The Astrophysical Journal, 728:122 (8pp), 2011 February 20 doi:10.1088/0004-637X/728/2/122
© 2011. The American Astronomical Society. All rights reserved. Printed in the U.S.A.

COSMIC-RAY PROTON AND HELIUM SPECTRA FROM THE FIRST CREAM FLIGHT

Y. S. Yoon[1,2], H. S. Ahn[1], P. S. Allison[3], M. G. Bagliesi[4], J. J. Beatty[3], G. Bigongiari[4], P. J. Boyle[5,11], J. T. Childers[6,12], N. B. Conklin[7,13], S. Coutu[7], M. A. DuVernois[6], O. Ganel[1], J. H. Han[1], J. A. Jeon[8], K. C. Kim[1], M. H. Lee[1], L. Lutz[1], P. Maestro[4], A. Malinine[1], P. S. Marrocchesi[4], S. A. Minnick[9], S. I. Mognet[7,14], S. Nam[8], S. Nutter[10], I. H. Park[8], N. H. Park[5,8], E. S. Seo[1,2], R. Sina[1], S. Swordy[5], S. P. Wakely[5], J. Wu[1], J. Yang[8], R. Zei[4], and S. Y. Zinn[1,15]

[1] Institute of Physical Science and Technology, University of Maryland, College Park, MD 20742, USA
[2] Department of Physics, University of Maryland, College Park, MD 20742, USA; ysy@umd.edu
[3] Department of Physics, Ohio State University, Columbus, OH 43210, USA
[4] Department of Physics, University of Siena and INFN, Via Roma 56, 53100 Siena, Italy
[5] Enrico Fermi Institute and Department of Physics, University of Chicago, Chicago, IL 60637, USA
[6] School of Physics and Astronomy, University of Minnesota, Minneapolis, MN 55455, USA
[7] Department of Physics, Penn State University, University Park, PA 16802, USA
[8] Department of Physics, Ewha Womans University, Seoul 120–750, Republic of Korea
[9] Department of Physics, Kent State University, Tuscarawas, New Philadelphia, OH 44663, USA
[10] Department of Physics and Geology, Northern Kentucky University, Highland Heights, KY 41099, USA
Received 2010 April 19; accepted 2010 December 14; published 2011 January 28

ABSTRACT

Cosmic-ray proton and helium spectra have been measured with the balloon-borne Cosmic Ray Energetics And Mass experiment flown for 42 days in Antarctica in the 2004–2005 austral summer season. High-energy cosmic-ray data were collected at an average altitude of ∼38.5 km with an average atmospheric overburden of ∼3.9 g cm^{-2}. Individual elements are clearly separated with a charge resolution of ∼0.15 e (in charge units) and ∼0.2 e for protons and helium nuclei, respectively. The measured spectra at the top of the atmosphere are represented by power laws with a spectral index of -2.66 ± 0.02 for protons from 2.5 TeV to 250 TeV and -2.58 ± 0.02 for helium nuclei from 630 GeV nucleon^{-1} to 63 TeV nucleon^{-1}. They are harder than previous measurements at a few tens of GeV nucleon^{-1}. The helium flux is higher than that expected from the extrapolation of the power law fitted to the lower-energy data. The relative abundance of protons to helium nuclei is 9.1 ± 0.5 for the range from 2.5 TeV nucleon^{-1} to 63 TeV nucleon^{-1}. This ratio is considerably smaller than the previous measurements at a few tens of GeV nucleon^{-1}.

Key words: balloons – cosmic rays – instrumentation: detectors – ISM: abundances – methods: data analysis

1. INTRODUCTION

Cosmic rays are the product of energetic processes in the universe, and their interactions with matter and fields are the source of much of the diffuse gamma-ray, X-ray, and radio emissions that are observed. Therefore, the origin of cosmic rays and how they propagate have a major impact on our understanding of the universe. Supernova shock waves could provide the power required to sustain the galactic cosmic-ray intensity, but details of the acceleration mechanism are not completely understood. The shock acceleration mechanism is believed to be a prevalent process in astrophysical plasmas on all scales throughout the universe. It has been shown to work in the heliosphere, e.g., at planetary bow shocks, at interplanetary shocks in the solar wind, and at the solar wind termination shock.

It is characteristic of diffusive shock acceleration that the resulting particle energy spectrum is mostly the same for a wide range of shock properties. This energy spectrum, when corrected for leakage from the Galaxy, is consistent with the observed spectrum of Galactic cosmic rays. In the most commonly used form of the theory, the characteristic limiting energy is about $Z \times 10^{14}$ eV, where Z is the particle charge (Lagage & Cesarsky 1983). The observed composition should begin to change beyond about 10^{14} eV, the limiting energy for protons, and the Fe spectrum would start to steepen at an energy 26 times higher. In this scenario, protons would be the most dominant element at low energies, but heavier elements would become relatively more abundant at higher energies, at least up to the acceleration limit for iron.

Compelling evidence that supernova remnants (SNRs) are common sites for the shock acceleration of electrons comes from observations of non-thermal synchrotron radiation from several shell-type remnants (Koyama et al. 1995; Allen et al. 1997; LeBohec et al. 2000). Non-thermal X-ray spectra indicate the presence of very high energy electrons which, at least in the case of SN 1006, have energies $>2 \times 10^{14}$ eV (Koyama et al. 1995). These electrons were likely accelerated at the remnant because at this energy electrons cannot travel far from their origin before they are attenuated by synchrotron losses. There are other sources of particle acceleration that may also contribute to the cosmic-ray beam (Dermer 2001). Recent *Chandra* X-ray observations of *Tycho's* SNR have shown hot stellar debris keeping pace with an outward-moving shock wave indicated by high-energy electrons.

Semi-direct evidence for the acceleration of cosmic-ray protons could come in the form of gamma rays from pion decay (Ellison & Cassam-Chenaï 2005). Indeed, the observation of TeV gamma rays, possibly of π^0 -origin, from the SNR RX J1713.7−3946 (Enomoto et al. 2002; Aharonian

[11] Now at Physics Department, McGill University, Montréal, Québec H3A 2T8, Canada.
[12] Now at Universität Heidelberg, Kirchhoff-Institut für Physik, 69120 Heidelberg, Deutschland.
[13] Now at Gannon University, 109 University Square, Erie, PA 16541, USA.
[14] Now at Department of Physics and Astronomy, University of California, Los Angeles, CA 90095, USA.
[15] Now at Promogen, Inc., 9605 Medical Center Drive, Rockville, MD 20850, USA.

et al. 2007) may have revealed the first specific site where protons are accelerated to energies typical of the main cosmic-ray component. Their hadronic origin is yet to be confirmed, but the CANGAROO collaboration has shown that the energy spectrum of gamma-ray emission from SNR RX J1713.7−3946 matches that expected if the gamma rays are the decay products of neutral pions generated in p–p collisions. Although the proton scenario is favored because of the spectral shape, gamma rays may originate from either electrons or protons. A complete understanding of gamma-ray emission processes may need a broadband approach (Aharonian et al. 2006), using all the available measurements in different wavelength regions. Direct measurements of nuclear particle composition changes would provide strong corroborating evidence that shocks associated with shell-type SNRs provide the acceleration sites for cosmic rays.

Shock acceleration is the generally accepted explanation for the characteristic power-law feature of cosmic-ray energy spectra, although ground-based measurements have shown that the all-particle spectrum extends far beyond the highest energy thought possible for supernova shock acceleration. These measurements have also shown that the energy spectrum above 10^{16} eV is somewhat steeper than the spectrum below 10^{14} eV, which lends credence to the possibility of a different source. Of course, the "knee" structure might be related to energy-dependent leakage effects during the propagation process (Ptuskin & Zirakashvili 1993; Swordy 1995) or to other effects, such as reacceleration in the galactic wind (Völk & Zirakashvili 2003) and acceleration in pulsars (Bednarek & Protheroe 2002). Whether and how the spectral "knee" is related to the mechanisms of acceleration, propagation, and confinement are among the major current questions in particle astrophysics.

2. CREAM EXPERIMENT

The Cosmic Ray Energetics And Mass (CREAM) experiment (Seo et al. 2008) was designed and constructed to extend balloon and space-based direct measurements of cosmic-ray elemental spectra to the highest energy possible in a series of balloon flights. The detailed energy dependence of elemental spectra at very high energies, where the rigidity-dependent supernova acceleration limit could be reflected in composition change, provides a key to understanding the acceleration and propagation of cosmic rays. We report in this paper the proton and helium spectra as well as their ratios observed from the maiden flight of the CREAM payload in Antarctica. Results from the CREAM experiment such as the B/C ratio and heavy elemental spectra are discussed in elsewhere (Ahn et al. 2008, 2009a, 2010).

2.1. CREAM Flight 2004–2005

The first Long Duration Balloon (LDB) flight of the CREAM payload was launched from McMurdo Station, Antarctica on 2004 December 16. It subsequently circumnavigated the South Pole three times for a record-breaking duration of 42 days; the flight was terminated on 2005 January 27. The instrument float altitude remained between 37 and 40 km through most of the flight. The corresponding atmospheric overburden was 3.9 ± 0.4 g cm^{-2}. The diurnal altitude variation due to the Sun angle change was very small, <1 km, near the pole, i.e., at high latitude, which increased as the balloon spiraled out to lower latitudes (Seo et al. 2008). The temperature of the various instrument boxes stayed within the required operational range with daily variations of a few °C, consistent with the Sun angle. A total of 60 GB of data including $\sim 4 \times 10^7$ science events were collected.

The science instrument was supported by the command and data module developed by the NASA Wallops Flight Facility (WFF; Thompson & Stuchlik 2008). This is in contrast to typical LDB payloads which utilize the support instrumentation package provided by the Columbia Scientific Balloon Facility (CSBF). CREAM was the first LDB mission to transmit all the prime science and housekeeping data (up to 85 kbps) in near real-time through the Tracking and Data Relay Satellite System (TDRSS) via a high-gain antenna, in addition to having an onboard data archive. To fit the data into this bandwidth, science event records excluded information from channels that had levels consistent with their pedestal value. This "data sparsification" reduced the average high-energy shower event record size by nearly 95%. The science instrument was controlled from a science operation center at the University of Maryland throughout the flight after line-of-sight operations ended at the launch site. Primary command uplink was via TDRSS, with Iridium serving as backup whenever the primary link was unavailable due to schedule or traversing zones of exclusion. The nearly continuous availability of command uplink and data downlink allowed rapid response to changing conditions on the payload (e.g., altitude-dependent effects) throughout the flight. More details about flight operations and the data acquisition system are discussed elsewhere (Yoon et al. 2005a; Zinn et al. 2005).

2.2. CREAM Instrument

The instrument was designed to meet the challenging and conflicting requirements to have a large enough geometry factor to collect adequate statistics for the low flux of high-energy particles, and yet stay within the weight limit for near-space flights (Ahn et al. 2007a). It was comprised of a suite of particle detectors to determine the charge and energy of the very high energy particles. As shown schematically in Figure 1, the detector configuration included a timing charge detector (TCD), a transition radiation detector (TRD) with a Cerenkov detector (CD), a silicon charge detector (SCD), hodoscopes (HDS), and a tungsten/scintillating fiber calorimeter. Starting from the top, the TCD consists of two crossed layers of four 5 mm thick and 1.2 m long plastic scintillators (Ahn et al. 2009b). It defines the 2.2 m^2 sr trigger geometry and determines charge based on the fact that the incident particle enters the TCD before developing a shower in the calorimeter, and the backscattered albedo particles arrive several nanoseconds later. A layer of scintillating fibers, S3, located between the carbon target and the tungsten calorimeter provides a reference time.

The TRD determines the Lorentz factor for $Z \geqslant 3$ nuclei by measuring transition X-rays using thin-wall gas tubes. Transition radiation is produced when a relativistic particle traverses an inhomogeneous medium, in particular the boundary between materials of different dielectric properties. The TRD consists of a foam radiator and 16 layers of proportional tubes filled with a mixture of xenon (95%) and methane (5%) gas (Ahn et al. 2008). The CD between the two TRD sections provides low-energy particle rejection at the flight site, Antarctica, where the geomagnetic cutoff is low. It also provides additional charge identification.

The SCD is comprised of 380 μm thick Si sensors (Park et al. 2007a). It is segmented into pixels, each about 2.12 cm^2 in area to minimize multiple hits in a segment due to backscattered particles. The targets are comprised of blocks of densi-

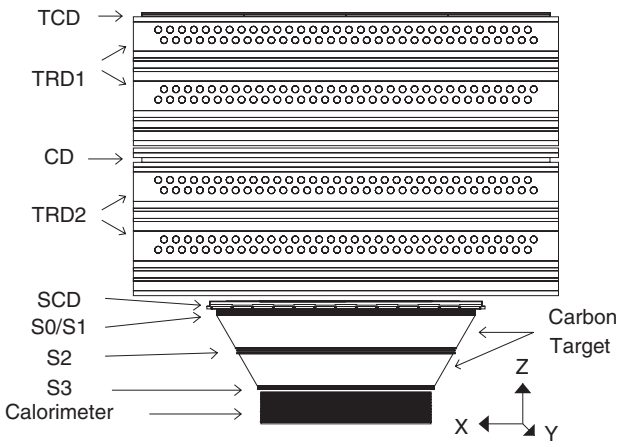

Figure 1. CREAM detector configuration. From the top are shown the TCD, upper TRD1, CD, lower TRD2, SCD, Hodoscope S0/S1, carbon targets, S2, S3, and the calorimeter.

fied graphite cemented in carbon/epoxy composite cradles. The vertical thickness of the carbon targets is about 0.5 interaction lengths. They force hadronic interactions in the calorimeter, which measures the shower energy and provides tracking information to determine which segment(s) of the charge detectors to use for the charge measurement (Seo et al. 1996).

The calorimeter consists of 20 tungsten layers interleaved with scintillating fiber ribbon layers which are alternately oriented in the x- and y-directions. Each tungsten layer is 1 radiation length thick to sample the shower every radiation length. Each layer consists of fifty 1 cm wide and 0.5 mm thick fiber ribbons to measure the longitudinal and lateral distributions of the shower. The light signal from each ribbon is collected by means of an acrylic light-mixer coupled to a bundle of clear fibers. This is split into three sub-bundles, each feeding a pixel of a hybrid photodiode (HPD). In this way the wide dynamic range of the calorimeter is divided into three sub-ranges (low, mid, high) with different gains, chosen to match the dynamic range of the front-end electronics (Lee et al. 2006). Tracking for showers is accomplished by extrapolating each shower axis back to the charge detectors. The HDS S0/S1 and S2, comprised of 2 mm thick and 2 mm wide scintillating fibers, provide additional tracking information above the tungsten stack (Yoon et al. 2005b; Marrocchesi et al. 2004). The tracking uncertainty is smaller than the pixel size of the SCD (Ahn et al. 2001).

Tracking for non-interacting particles is achieved in the TRD with better accuracy (1 mm resolution with 67 cm lever arm, 0.0015 radians). The TRD and calorimeter have different systematic biases in determining particle energy. The use of both instruments allows in-flight cross-calibration of the two techniques and, consequently, provides a powerful method for measuring cosmic-ray energies (Maestro et al. 2007). Details of the detectors and their performance are discussed elsewhere (Lee et al. 2006; Park et al. 2004; Ahn et al. 2007a).

3. DATA ANALYSIS

The main trigger conditions for science events were (1) significant energy deposit in the calorimeter for high-energy particles or (2) large pulse height, $Z > 2$, in the TCD for heavy nuclei. The former requires each of six consecutive layers in the calorimeter to have at least one ribbon recording a deposit of more than 45 MeV. The high-energy shower events that meet this calorimeter trigger condition were used in this analysis.

3.1. Event Selection

The ribbon with the highest energy deposit and the neighboring ribbons on both sides were used to determine the position in each layer of maximum energy deposits. The shower axis was reconstructed by a least-squares fit of a straight line through a combination of these hit positions in the XZ and YZ planes (Ahn et al. 2007b). Hits not along the straight line were excluded from the fit. The resulting trajectory resolution is ~1 cm when projected to the SCD. The reconstructed trajectories were required to traverse the SCD active area and the bottom of the calorimeter active area.

At this stage non-interacting particles are removed, but some events have their first hadronic interaction in the calorimeter layers instead of the carbon targets. These late interacting events could result in an underestimation of deposited energy or misidentification of charge due to large uncertainties in the trajectory reconstruction. Since their longitudinal shower profiles are different, events with small energy deposit in the top few layers of the calorimeter were removed to ensure that the selected events had their first interactions either in the carbon targets or in the top of the calorimeter.

3.2. Charge Determination

In order to determine the incident particle charge, the reconstructed shower axis from the calorimeter was extrapolated to the SCD and a 7×7 pixel area, about 10×10 cm^2, centered on the extrapolated position, was scanned to seek for the highest pixel signal. The scanned area was optimized to sustain the charge identification efficiency of 99% in all energy bins, accounting for dead and noisy SCD and calorimeter channels (~15% and 13%, respectively), and determined to be a 7×7 pixel area. That highest pixel signal was then corrected for the particle path length (calculated from the reconstructed incidence angle) in the sensor. The signal reflects the ionization energy loss per unit path length (dE/dx) of an incident particle in the SCD. The energy loss is proportional to Z^2. According to Monte Carlo (MC) simulations and beam tests, the expected contamination from secondary particles backscattering from the calorimeter is <3% when this tracking-based selection method is used (Park et al. 2007b). The resulting SCD signal distribution is shown in Figure 2. Events with $Z < 1.7$ were selected as protons, while events with $1.7 \leqslant Z < 2.7$ were selected as helium nuclei. The charge resolutions are estimated as ~0.15 e and ~0.2 e for protons and helium nuclei, respectively. The proton and helium losses due to dE/dx Landau tails were corrected by charge selection efficiencies, which will be discussed in Section 3.6. The proton events in the helium range were removed as a background in the helium selection, and the helium events in the proton range were removed as a background in the proton selection, which will be discussed in Section 3.5. Unstable SCD channels identified by their large root-mean-square pedestal variations throughout the flight were excluded from the analysis. Including dead or noisy channels, ~15% of the total 2912 SCD channels were masked.

3.3. Energy Measurement

An ionization calorimeter is the only practical way to measure the energy of protons and helium nuclei above ~1 TeV, but calorimeters with full containment of hadronic showers are too massive to be incorporated into space-based or balloon-borne experiments (Ganel et al. 1999). A thin calorimeter offers a practical approach but the calorimeter calibration requires

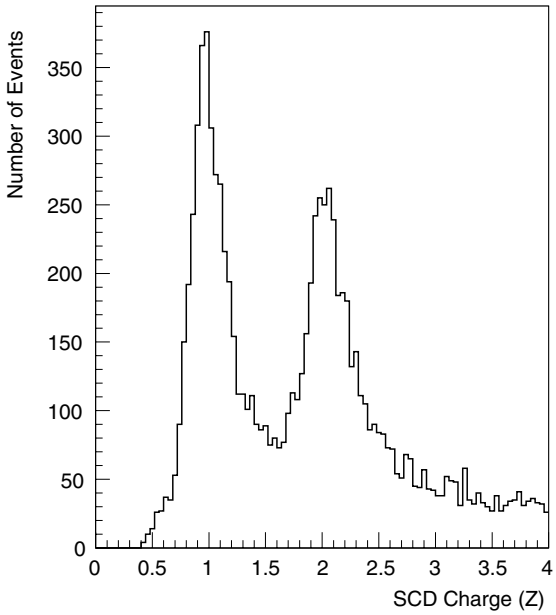

Figure 2. Charge distribution of selected events determined with the SCD. The number of protons and helium nuclei are identified from the charge distribution in each energy bin.

the use of accelerator beam particles having known energy. The CREAM calorimeter was calibrated before the flight with electron beams at the European Organization for Nuclear Research (CERN). Each of the 1000 fiber ribbons was exposed to 150 GeV electrons. The responses from the 50 ribbons in a given layer are equalized by moving the detector in steps of 1 cm vertically or 1 cm horizontally, so the electron beam is centered each time on the center of a different ribbon in each X or Y layer.

The calorimeter was designed to measure the energy deposit from showers initiated by nuclei with energies up to 10^{15} eV and higher. Its sampling fraction for isotropically incident TeV proton showers initiated in the graphite targets is about 0.13% of the parent's energy in the active media. With electron test beam energies of 150 GeV or less, only 8–10 layers around the shower maximum register enough scintillation to allow calibration. To address this, the calibration scan was carried out in three sets of runs by exposing the calorimeter from the bottom with additional targets along the beam line as described in Ahn et al. (2007a).

The energy deposit expected along the shower core in each layer was calculated using MC simulations of electron showers. Conversion factors from analog-to-digital conversion (ADC) signals to MeV were obtained from the ratio of MC simulation of the energy deposited in each ribbon to the measured ADC signal from the calibration beam test. The MC simulations were based on GEANT/FLUKA 3.21 (Brun et al. 1984; Fasso et al. 1993). The ADC signals were corrected for the HPD quantum efficiency and gain difference from the different HPD high-voltage settings between the beam test and the flight.

Inter-calibration between the low- and mid- energy ranges and between the mid- and high-energy ranges were carried out with flight data by comparing the signals from two ranges of the same ribbon generated by the same shower. None of the proton and helium event candidates saturated in the middle range, so the high range optical division was not needed for this analysis. More details about the calibration can be found in Yoon et al. (2005c, 2007) and Ahn et al. (2006a).

The calorimeter, HDS, and SCD were also exposed to nuclear fragments (A/Z = 2) of a 158 GeV nucleon^{-1} Indium beam at CERN (Yoon et al. 2007; Ahn et al. 2006a; Marrocchesi et al. 2004; Park et al. 2004). The energy response was linear up to the maximum beam energy of ∼9 TeV. Above the available accelerator beam energy, MC simulations indicate that the calorimeter response is quite linear in the CREAM measurement energy range. Simulations also indicate that the calorimeter energy resolution is nearly energy independent (Ahn et al. 2001). Nevertheless, our energy deconvolution included corrections for the small energy dependence of the energy resolution due to shower leakage (Ahn et al. 2009a).

3.4. Spectral Deconvolution

Entries in the deposited energy bins were deconvolved into incident energy bins using matrix relations. The counts, $N_{\mathrm{inc,i}}$, in incident energy bin i were estimated from the measured counts, $N_{\mathrm{dep,j}}$, in deposited energy bin j by the relation (Buckley et al. 1994; Ahn et al. 2006b)

$$N_{\mathrm{inc,\,i}} = \sum_j P_{ij} N_{\mathrm{dep,\,j}}, \quad (1)$$

where matrix element P_{ij} is the probability that the events in the deposited energy bin j are from incident energy bin i. The matrix element P_{ij} was estimated from the response matrix generated by MC simulation results obtained separately for protons and helium nuclei. The response matrix and corresponding deconvolution matrix were generated and tested by varying the indices between −2.5 and −2.8. We verified that the flux deconvolution process was not sensitive to the assumed spectral index used, within that range, to generate the matrix elements.

The MC simulations for helium and heavy nuclei used FRITIOF/RQMD/DPMJET-II (Kim et al. 1999; Wang et al. 2001) interfaced to the GEANT/FLUKA 3.21 hadronic simulation package. FRITIOF (Andersson et al. 1993) is based upon semiclassical considerations of string dynamics for high-energy hadronic collisions. The relativistic quantum molecular dynamics (RQMD) model was adopted for simulations of heavy ions for energies in the center-of-mass frame less than 5 GeV nucleon^{-1}. RQMD is a semiclassical microscopic approach which combines classical propagation with stochastic interactions (Sorge 1995). DPMJET-II (Ranft 1995; Ferrari et al. 1996) was based on the dual parton model, a framework for hadron–hadron interactions and production in hadron–nucleus and nucleus–nucleus collisions at high energies.

3.5. Background Corrections

The primary background is comprised of events with misidentified charge, which result mainly from secondary particles generated by interactions above the SCD or from particles backscattered from the calorimeter. This is the case for the protons; however, there is an additional cause of misidentified events for helium nuclei: the proton dE/dx Landau tail. Misidentified event counts of protons and helium nuclei were estimated from the MC simulations with a power-law input spectrum. Due to the Landau tails, backscattered and secondary particles, 5.1% of measured protons were misidentified helium nuclei and 6.8% of measured helium nuclei were misidentified protons, as shown in Table 1. About 0.2% of incident carbon nuclei were identified as protons, and 2.8% of incident carbon nuclei were misidentified as helium nuclei, using the energy spectra of individual cosmic-rays compiled by Wiebel-Sooth et al. (1998). Less than

Table 1
Efficiencies and Backgrounds for Absolute Flux

Efficiency and Background	Proton (%)	Helium (%)
Trigger efficiency	76 ± 2	91 ± 1
Reconstruction efficiency	98 ± 1	99 ± 1
Late interaction events efficiency	90 ± 1	96 ± 1
Charge selection efficiency	77 ± 2	67 ± 2
Background from reconstruction	3.6 ± 0.1	4.0 ± 0.2
Background from misidentified charge	5.1 ± 0.2	6.8 ± 0.2

1% of trigger and reconstructed protons and helium events are from secondary particles. Additional background comes from the events that are not within the geometry, but which satisfy the trigger and reconstruction conditions; they are either entering the instrument acceptance from outside the SCD area or exiting the side of the calorimeter instead of the bottom. According to MC simulations, this is about 3.6% and 4.0% of the selected events for protons and helium nuclei, respectively. The total background was 9% for protons and 11% for helium nuclei.

3.6. Absolute Flux

The measured spectra are corrected for the instrument acceptance as shown below to obtain the absolute flux F:

$$F = \frac{dN}{dE}\frac{1}{GF\varepsilon T\eta}, \tag{2}$$

where dN is the number of events in an energy bin, dE is the energy bin size, GF is the geometry factor, ε is the efficiency (defined below), T is the live time, and η is the survival fraction after accounting for atmospheric attenuation. The geometry factor was calculated to be 0.43 m^2 sr using an MC simulations by requiring the extrapolated calorimeter trajectory of the incident particle to traverse the SCD active area and the bottom of the calorimeter. Out of 42 days of the flight, the stable period was about 24 days when no commands were sent, e.g., for instrument tuning, power-cycle, or high-voltage adjustments. After the dead-time correction, the live time, T, of 1,099,760 s was used for this analysis.

Efficiency. The efficiency, ε in Equation (2), includes efficiencies from all analysis steps, including trigger condition, event reconstruction, charge identification, and removing events with late interactions:

$$\varepsilon = \varepsilon_{\rm trig}\varepsilon_{\rm rec}\varepsilon_{\rm sel}\varepsilon_{\rm charge}\,. \tag{3}$$

The trigger efficiency, $\varepsilon_{\rm trig}$, was obtained from the fraction of events satisfying the trigger condition among all events within the geometry, i.e., passing through the bottom of the calorimeter and the SCD active area, using MC simulations. This is energy dependent at low energies where the trigger is not fully efficient. Above 3 TeV, it is nearly constant around 76% for protons and 91% for helium nuclei, respectively. The reconstruction efficiency, $\varepsilon_{\rm rec}$, was taken to be the ratio of events satisfying the reconstruction and trigger conditions to events satisfying only the trigger condition. The reconstruction efficiency was 98% for protons and 99% for helium nuclei, respectively, based on MC simulations. The event selection efficiency, $\varepsilon_{\rm sel}$, was estimated with the MC simulations after removing events with late interactions and was 90% protons and 96% for helium nuclei. The charge efficiency, $\varepsilon_{\rm charge}$, takes into account lost events due to the noisy or dead SCD channels, interactions above SCD, and misidentified charges. It was calculated to be 77% for protons and 67% for helium nuclei, respectively, using MC simulations. The efficiencies are summarized in Table 1.

The trigger efficiency for proton and helium nuclei cannot be estimated with the flight data, since we do not know how many un-triggered events occurred. However, the event selection efficiency, $\varepsilon_{\rm sel}$, and charge efficiency, $\varepsilon_{\rm charge}$, were estimated in a limited way using flight data for combined protons and helium nuclei events. It is not as accurate as individual MC simulations because the composition (abundance) of the incident particles is unknown. When the abundance ratio of protons and helium nuclei was assumed to be 1:1 and the abundance of heavy nuclei above helium nuclei was ignored, the combined efficiencies were 68% from the flight data and 67% for the MC simulations.

Interactions in air. The attenuation loss due to the atmospheric overburden, 3.9 ± 0.4 g cm^{-2}, was corrected for survival fractions of protons and helium nuclei. This air depth was measured by pressure sensors during the flight. Interaction cross sections have been measured in many fixed target experiments, and cross sections are known up to a few tens of GeV (Hagen et al. 1977; Webber et al. 1990; Papini et al. 1996). We used the cross section formula from Hagen et al. (1977) to calculate interaction lengths and survival fractions for protons and helium nuclei. The mean incident angle of 35°, estimated from the flight data, was used to estimate the losses. The survival fraction, η, used to characterize atmospheric attenuation was determined to be 95% for protons and 91% for helium nuclei, respectively.

The ratio of secondary to primary protons and helium nuclei in the atmosphere above GeV energies has been reported (Kawamura et al. 1989; Abe et al. 2003). Papini et al. (1996) calculated that the secondary to primary proton ratio at an air depth of 3 g cm^{-2} was less than 1% above 40 GeV, and the secondary to primary helium nuclei ratio was less than 2% at 10 GeV $nucleon^{-1}$. Our MC simulations showed that the fraction of secondary protons and helium nuclei produced from carbon and iron nuclei interactions in the air was less than 1% at 10 TeV.

Energy-bin representation. For the number of events (dN) in each energy bin with upper- and lower-energy limits, E_{j+1} and E_j, respectively ($dE = E_{j+1} - E_j$), the differential flux is dN/dE at E_m, where E_m can be taken as the arithmetic mean of E_j and E_{j+1} in logarithmic range or else using a suitably weighted average of E_j and E_{j+1}. We also investigated an alternative procedure to determine E_m, as suggested by Lafferty & Wyatt (1995):

$$f(E_m) = \frac{1}{E_{j+1} - E_j}\int_{E_j}^{E_{j+1}} f(E)dE. \tag{4}$$

For a power-law spectrum, $f(E) = AE^{-\gamma}$, E_m can be calculated as

$$E_m = \left(\frac{E_{j+1}^{1-\gamma} - E_j^{1-\gamma}}{(E_{j+1} - E_j)(1-\gamma)}\right)^{-1/\gamma}. \tag{5}$$

In this analysis, E_m was used and the difference between E_m and the center of the bin in logarithmic range is less than 1%.

3.7. Uncertainties

The statistical uncertainty in each energy bin was estimated by the relation $\delta N_{\rm inc,i} = \delta(\sum_j P_{ij} N_{\rm dep,j})$, considering 68.3% to be the Poisson confidence interval determined by Feldman & Cousins (1998). The uncertainties were estimated by propagating uncertainties of measured entries in each bin and uncertainties of deconvolution components, P_{ij}, from MC simulations,

Table 2
Proton Differential Flux Measured with CREAM

Energy Bin Range (GeV)	Flux ± Stat. $(m^2\ sr\ s\ GeV)^{-1}$
2.5×10^3–4.0×10^3	$(3.72\pm0.10)\times10^{-6}$
4.0×10^3–6.3×10^3	$(1.10\pm0.04)\times10^{-6}$
6.3×10^3–1.0×10^4	$(3.19\pm0.19)\times10^{-7}$
1.0×10^4–1.6×10^4	$(9.47\pm0.80)\times10^{-8}$
1.6×10^4–2.5×10^4	$(2.80\pm0.35)\times10^{-8}$
2.5×10^4–4.0×10^4	$(8.1\pm1.5)\times10^{-9}$
4.0×10^4–6.3×10^4	$(2.2\pm0.6)\times10^{-9}$
6.3×10^4–1.0×10^5	$(6.1^{+2.6}_{-2.2})\times10^{-10}$
1.0×10^5–1.6×10^5	$(1.8^{+1.2}_{-0.9})\times10^{-10}$
1.6×10^5–2.5×10^5	$(4.2^{+5.4}_{-3.4})\times10^{-11}$

Table 3
Helium Differential Flux Measured with CREAM

Energy Bin Range (GeV nucleon^{-1})	Flux ± Stat. $(m^2\ sr\ s\ GeV\ nucleon^{-1})^{-1}$
6.3×10^2–1.0×10^3	$(1.42\pm0.04)\times10^{-5}$
1.0×10^3–1.6×10^3	$(4.35\pm0.16)\times10^{-6}$
1.6×10^3–2.5×10^3	$(1.31\pm0.07)\times10^{-6}$
2.5×10^3–4.0×10^3	$(3.83\pm0.31)\times10^{-7}$
4.0×10^3–6.3×10^3	$(1.27\pm0.14)\times10^{-7}$
6.3×10^3–1.0×10^4	$(4.19\pm0.64)\times10^{-8}$
1.0×10^4–1.6×10^4	$(1.15\pm0.27)\times10^{-8}$
1.6×10^4–2.5×10^4	$(3.4^{+1.1}_{-1.0})\times10^{-9}$
2.5×10^4–4.0×10^4	$(8.2^{+4.9}_{-3.8})\times10^{-10}$
4.0×10^4–6.3×10^4	$(2.9^{+2.4}_{-1.5})\times10^{-10}$

while in the paper reported by Ahn et al. (2010), uncertainties were estimated by propagating uncertainties from measured entries with P_{ij}. This estimation gives more conservative results than the reported results.

Several sources of systematic uncertainties were identified. The systematic uncertainties for efficiencies and backgrounds were estimated within each energy range to account for the energy-dependent effects determined using MC simulations. They are summarized in Table 1. Efficiency uncertainties were about 1%–2%, and background uncertainties were about 5%.

The geometry factor uncertainty was 2% for both protons and helium nuclei; it was estimated with MC simulations. The precision of estimated live-time fraction was about 3.3% and the accuracy of estimated dead time due to timeouts in TCD readout, which delayed processing, was about 2.6%. The overall uncertainties for the estimated live time were 4% for both protons and helium nuclei. The systematic uncertainties for the survival fractions in the atmosphere were calculated analytically. The p–p cross section difference between 10 TeV and 100 TeV is about 28%, according to the most recent reference from the Particle Data Group (Amsler et al. 2008). Using a conservative estimate of 30% for cross section uncertainties, the estimated uncertainties of survival fractions were 2% and 3% for protons and helium nuclei, respectively. The range of incident angle was from 0° to 66°. The uncertainty in correcting for atmospheric losses introduced by using an assumed mean incident angle was at the level of 1% for protons and 1.6% for helium nuclei. The energy calibration accuracy was found to be 1%. The systematic uncertainties of the measured number in each energy bin, considering the 1% energy calibration accuracy, were 3% for both protons and helium nuclei. To estimate uncertainties in the spectral deconvolution, the unfolding procedure was repeated by varying input spectral indices. The difference of the proton fluxes varying the input spectral indices between 2.64 and 2.68 was less than 1%. Similarly, the helium flux difference was also less than 1% for input spectra between indices 2.56 and 2.60. The overall systematic uncertainties were found to be 9% for both protons and helium nuclei. These systematic uncertainties are energy independent. They do not change the spectral shape, but they might shift the normalization of the spectra up or down.

4. RESULTS

The measured proton fluxes from 2.5 TeV to 250 TeV and helium fluxes from 630 GeV nucleon^{-1} to 63 TeV nucleon^{-1} at the top of the atmosphere are given in Tables 2 and 3, while previously reported results in the paper by Ahn et al. (2010) are presented in a plot. The statistical uncertainties were re-estimated, as discussed in Section 3.7. The CREAM proton and helium spectra are each consistent with a single power law over the measured range. The best-fit parameters for the spectra for protons and helium nuclei are represented by

$$\frac{d\Phi}{dE} = \Phi_0 E^{-\beta} (\mathrm{m^2\ sr\ s\ GeV\ nucleon^{-1}})^{-1}. \quad (6)$$

The best-fit parameters for the spectra for protons and helium nuclei are given by Ahn et al. (2010):

$$\Phi_{0,p} = (7.8\pm1.9)\times10^3 (\mathrm{m^2\ sr\ s})^{-1} (\mathrm{GeV\ nucleon^{-1}})^{1.66}, \quad (7)$$

$$\beta_p = 2.66\pm0.02, \quad (8)$$

and

$$\Phi_{0,\mathrm{He}} = (4.2\pm0.8)\times10^2 (\mathrm{m^2\ sr\ s})^{-1}\ (\mathrm{GeV\ nucleon^{-1}})^{1.58}, \quad (9)$$

$$\beta_{\mathrm{He}} = 2.58\pm0.02. \quad (10)$$

The spectral indices for proton and helium nuclei were calculated both with the least-squares fit and maximum likelihood method. The results from both methods were consistent. Uncertainties for the spectral indices were estimated with the maximum likelihood method.

The CREAM proton spectrum is harder than previous measurements at lower energies such as AMS (Aguilar et al. 2002), 2.78 ± 0.009 at 10–200 GV, and BESS (Haino et al. 2004), 2.732 ± 0.011 from 30 GeV to a few hundred GeV. Likewise, the CREAM helium spectrum is harder than AMS, 2.740 ± 0.01 at 20–200 GV and BESS, 2.699 ± 0.040 from 20 GeV nucleon^{-1} to a few hundred GeV nucleon^{-1}.

Figure 3 compares our measured spectra with previous measurements: AMS, BESS, CAPRICE98 (Boezio et al. 2003), ATIC-2 (Panov et al. 2009), JACEE (Asakimori et al. 1998), and RUNJOB (Derbina et al. 2005). The error bars shown in the figures represent the statistical uncertainties. The CREAM results are consistent with JACEE where its measurement energy range overlaps with CREAM but indicate higher fluxes, particularly for helium, with respect to RUNJOB. The proton and helium fluxes are both higher than that expected by extrapolating the power law fitted to the lower-energy measurements, which verifies that our TeV spectra are harder than the lower-energy spectra. At 20 TeV nucleon^{-1} the helium flux measured by CREAM is about 4σ higher than the flux expected from a power-law extrapolation of the AMS helium flux and spectral index.

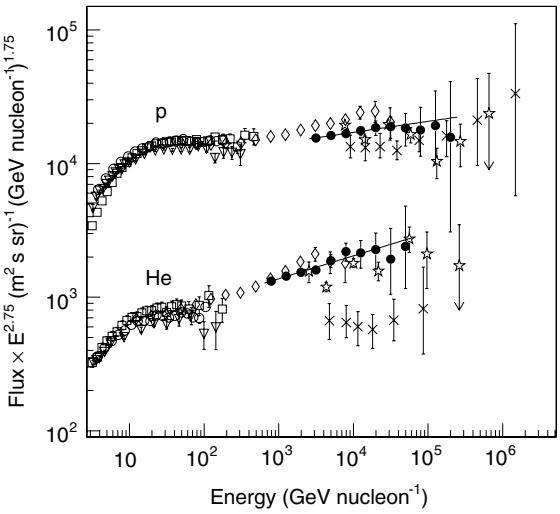

Figure 3. CREAM proton and helium differential $Flux \cdot E^{2.75}$ in GeV nucleon^{-1} at the top of the atmosphere. The CREAM proton and helium spectra (filled circles) are shown together with previous measurements: BESS (squares), CAPRICE98 (downward triangles), AMS (open circles), ATIC-2 (diamonds), JACEE (stars), and RUNJOB (crosses). The lines represent power-law fits with spectral indices of -2.66 ± 0.02 for protons and -2.58 ± 0.02 for helium nuclei, respectively.

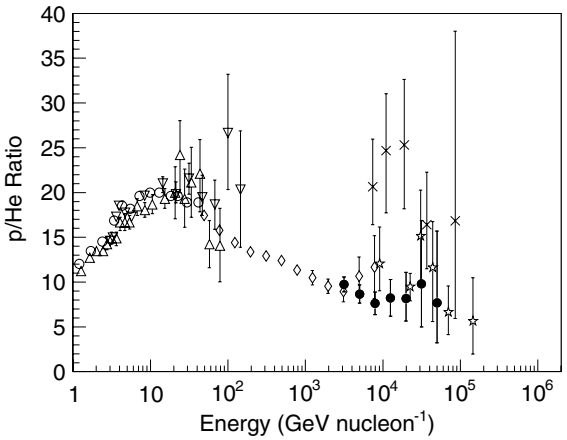

Figure 4. Ratio of protons to helium nuclei as a function of energy in GeV nucleon^{-1}. The CREAM (filled circles) ratio of proton to helium is compared with previous measurements: ATIC-2 (diamonds), CAPRICE94 (upward triangles), CAPRICE98 (downward triangles), LEAP (open circles), JACEE (stars), and RUNJOB (crosses).

The proton to helium ratio as a function of energy provides insight into whether the proton and helium spectra have the same spectral index. This has long been a tantalizing question, mainly because of the limited energy range individual experiments could cover. The ratio from the first CREAM flight provides a much needed higher energy, low-statistical uncertainty, measurement. The ratio is compared with previous measurements in Figure 4: ATIC-2, CAPRICE94 (Boezio et al. 1999), CAPRICE98, JACEE (Asakimori et al. 1993b), LEAP (Seo et al. 1991), and RUNJOB. The CREAM ratios are consistent with JACEE where its measurement energy range overlaps. The measured CREAM ratio at the top of the atmosphere is on average 9.1 ± 0.5 for the range from 2.5 TeV nucleon^{-1} to 63 TeV nucleon^{-1}, which is significantly lower than the ratio of $\sim$20 obtained from the lower-energy measurements.

5. DISCUSSION AND CONCLUSION

The energy spectra of primary cosmic rays are known with good precision up to energies around 10^{11} eV, where magnetic spectrometers have been able to carry out such measurements. Above this energy the composition and energy spectra are not accurately known, although there have been some pioneering measurements (Müller et al. 1991; Asakimori et al. 1998; Apanasenko et al. 2001). The collecting power of CREAM is about a factor of two larger than that of ATIC for protons and helium nuclei and, considering the much larger geometry factor of the TRD, about a factor of 10 larger for heavier nuclei. TRACER has a larger geometry factor than CREAM, but a smaller dynamic charge range ($Z = 8$–26) was reported for its 10 day Antarctic flight. Although its dynamic charge range was improved to $Z = 3$–26 for its $\sim$4 day flight from Sweden to Canada in 2006, it is still insensitive to protons and helium nuclei.

The CREAM payload maintained a high altitude, corresponding to an atmospheric overburden of 3.9 g cm^{-2} for vertically incident particles. That implies about 6.8 g cm^{-2} at the maximum acceptance angle for this analysis, which is the smallest among comparable experiments. For example, the average vertical depth for RUNJOB was more than twice that of CREAM, due to its low flight altitude. Considering the RUNJOB acceptance of particles at large zenith angles, its effective atmospheric depth was as large as 50 g cm^{-2}. For that depth, large corrections are required to account for the fact that 41% of protons would have interacted before reaching the detector.

The CREAM calorimeter is much deeper than either that of JACEE or RUNJOB, so it provides better energy measurements. CREAM also has excellent charge resolution, sufficient to clearly identify individual nuclei, whereas JACEE and RUNJOB reported elemental groups. Our observation did not confirm a softer spectrum of protons above 2 TeV reported by Grigorov et al. (1970) or a bend around 40 TeV (Asakimori et al. 1993a). An increase in the flux of helium relative to protons could be interpreted as evidence for two different types of sources for protons and helium nuclei as proposed by Biermann (1993). The observed harder spectra compared to prior low-energy measurements may require a significant modification of conventional acceleration and propagation models, with significant impact for the interpretation of other experimental observations.

The CREAM experiment was planned for Ultra Long Duration Balloon (ULDB) flights lasting about 100 days with super-pressure balloons. While waiting for development of these exceptionally long flights, the CREAM instrument has flown five times on LDB flights in Antarctica. It should be noted that a 7 million cubic foot ($\sim$0.2 million cubic meters) super-pressure balloon was flown successfully for 54 days during the 2008–2009 austral summer season. As ULDB flights become available for large science payloads, long-duration exposures can be achieved faster and more efficiently with reduced payload refurbishment and launch efforts. Whatever the flight duration, data from each flight reduces the statistical uncertainties and extends the reach of measurements to energies higher than previously possible.

This work was supported in the U.S. by NASA grants NNX07AN54H, NNX08AC11G, NNX08AC15G, NNX08AC16G, and their predecessor grants, in Italy by INFN, and in Korea by the Creative Research Initiatives of MEST/NRF. The authors wish to acknowledge NASA/WFF for

provision and operation of flight support systems; CERN for provision of excellent accelerator beams; and CSBF, National Science Foundation's Office of Polar Programs, and Raytheon Polar Services Company for outstanding support of launch, flight, and recovery operations in Antarctica.

REFERENCES

Abe, K., et al. 2003, Phys. Lett. B, 564, 8
Aguilar, M., et al. 2002, Phys. Rep., 366, 331
Aharonian, F., et al. 2006, A&A, 449, 223
Aharonian, F., et al. 2007, A&A, 464, 235
Ahn, H. S., et al. 2001, Proc. 27th ICRC (Pune), Vol., 6, 2159
Ahn, H. S., et al. 2006a, Nucl. Phys. B, 150, 272
Ahn, H. S., et al. 2006b, Adv. Space Res., 37, 1950
Ahn, H. S., et al. 2007a, Nucl. Instrum. Methods Phys. Res. A, 579, 1034
Ahn, H. S., et al. 2007b, Proc. 30th ICRC (Merida), Vol., 2, 63
Ahn, H. S., et al. 2008, Astropart. Phys., 30, 133
Ahn, H. S., et al. 2009a, ApJ, 707, 593
Ahn, H. S., et al. 2009b, Nucl. Instrum. Methods. A, 602, 525
Ahn, H. S., et al. 2010, ApJ, 714, L89
Allen, G. E., et al. 1997, ApJ, 487, L97
Amsler, C., et al. 2008, Phys. Lett. B, 667, 1
Andersson, B., Gustafson, G., & Pi, H. 1993, Z. Phys. C Part. Fields, 57, 485
Apanasenko, A. V., et al. 2001, Astropart. Phys., 16, 13
Asakimori, K., et al. 1993a, Proc. 23rd ICRC (Calgary), Vol., 2, 21
Asakimori, K., et al. 1993b, Proc. 23rd ICRC (Calgary), Vol., 2, 25
Asakimori, K., et al. 1998, ApJ, 502, 278
Bednarek, W., & Protheroe, R. J. 2002, Astropart. Phys., 16, 397
Biermann, P. L. 1993, A&A, 271, 649
Boezio, M., et al. 1999, ApJ, 518, 457
Boezio, M., et al. 2003, Astropart. Phys., 19, 583
Brun, R., Bruyant, F., Maire, M., McPherson, A. C., & Zanarini, P. 1984, GEANT User Guide, CERN DD/EE/84-1, Geneva
Buckley, J., Dwyer, J., Müller, D., Swordy, S., & Tang, K. K. 1994, ApJ, 429, 736
Derbina, V. A., et al. 2005, ApJ, 628, L41
Dermer, C. D. 2001, Proc. 27th ICRC (Hamburg), Vol., 6, 2039
Ellison, D. C., & Cassam-Chenaï, G. 2005, ApJ, 632, 920
Enomoto, R., et al. 2002, Nature, 416, 823
Fasso, A., Ferrari, A., Ranft, J., & Sala, P. R. 1993, in Proc. IV Int. Conf. on Calorimetry in High Energy Physics, La Biodola, Italy, ed. A. Menzione & A. Scribano (Singapore: World Scientific), 493
Feldman, G. J., & Cousins, R. D. 1998, Phys. Rev. D, 57, 3873
Ferrari, A., Ranft, J., Roesler, S., & Sala, P. R. 1996, Z. Phys. C Part. Fields, 71, 75
Ganel, O., Seo, E. S., & Wang, Z. 1999, Proc. 26th ICRC (Salt Lake), Vol., 5, 33
Grigorov, N. L., Nesterov, V. E., Rapoport, I. D., Savenko, I. A., & Skuridin, G. A. 1970, Sov. J. Nucl. Phys., 11, 1058
Hagen, F. A., Fisher, A. J., & Ormes, J. F. 1977, ApJ, 212, 262
Haino, S., et al. 2004, Phys. Lett. B, 594, 35
Kawamura, Y., et al. 1989, Phys. Rev. D, 40, 729
Kim, H. J., et al. 1999, Proc. 26th ICRC (Salt Lake), Vol., 1, 17
Koyama, K., Petre, R., Gotthelf, E. V., Hwang, U., Matsuura, M., Ozaki, M., & Holt, S. S. 1995, Nature, 378, 255
Lafferty, G. D., & Wyatt, T. R. 1995, Nucl. Instrum. Methods. A, 355, 541
Lagage, P. O., & Cesarsky, C. J. 1983, A&A, 125, 249
LeBohec, S., et al. 2000, ApJ, 539, 209
Lee, M. H., et al. 2006, in AIP Conf. Ser. 867, Calorimetry in High Energy Physics: XII, ed. S. R. Magill & R. Yoshida (Melville, NY: AIP), 167
Maestro, P., et al. 2007, Proc. 30th ICRC (Merida), Vol., 2, 333
Marrocchesi, P. S., et al. 2004, Nucl. Phys. B, 134, 75
Müller, D., Swordy, S. P., Meyer, P., L'Heureux, J., & Grunsfeld, J. M. 1991, ApJ, 374, 356
Panov, A. D., et al. 2009, Bull. Russ. Acad. Sci. Phys., 73, 564
Papini, P., Grimani, C., & Stephens, S. A. 1996, Nuovo Cimento C, 19, 367
Park, I. H., et al. 2004, Nucl. Instrum. Methods. A, 535, 158
Park, I. H., et al. 2007a, Nucl. Instrum. Methods. A, 570, 286
Park, N. H., et al. 2007b, Proc. 30th ICRC (Merida), Vol., 2, 381
Ptuskin, V. S., & Zirakashvili, V. N. 1993, Proc. 23rd ICRC (Calgary), Vol., 2, 290
Ranft, J. 1995, Phys. Rev. D, 51, 64
Seo, E., et al. 1996, Proc. SPIE, 2806, 134
Seo, E. S., Ormes, J. F., Streitmatter, R. E., Stochaj, S. J., Jones, W. V., Stephens, S. A., & Bowen, T. 1991, ApJ, 378, 763
Seo, E. S., et al. 2008, Adv. Spa. Res., 42, 1656
Sorge, H. 1995, Phys. Rev. C, 52, 3291
Swordy, P. S. 1995, Proc. 24th ICRC (Rome), Vol., 2, 697
Thompson, L. D., & Stuchlik, D. W. 2008, Adv. Spa. Res., 42, 1698
Völk, H. J., & Zirakashvili, V. N. 2003, Proc. 28th ICRC (Tsukuba), Vol., 4, 2031
Wang, J. Z., et al. 2001, Proc. 27th ICRC (Hamburg), Vol., 4, 1445
Webber, W. R., Kish, J. C., & Schrier, D. A. 1990, Phys. Rev. C, 41, 520
Wiebel-Sooth, B., Biermann, P. L., & Meyer, H. 1998, A&A, 330, 389
Yoon, Y. S., et al. 2005a, Proc. 29th ICRC (Pune), Vol., 3, 429
Yoon, Y. S., et al. 2005b, Proc. 29th ICRC (Pune), Vol., 3, 433
Yoon, Y. S., et al. 2005c, Proc. 29th ICRC (Pune), Vol., 8, 371
Yoon, Y. S., et al. 2007, Proc. 30th ICRC (Merida), Vol., 2, 421
Zinn, S. Y., et al. 2005, Proc. 29th ICRC (Pune), Vol., 3, 437